

# Mechanical aspects of thrust faulting driven by far-field compression and their implications for fold geometry

Pablo F. Sanz · Ronaldo I. Borja · David D. Pollard

Received: 21 December 2006 / Accepted: 23 February 2007 / Published online: 18 April 2007  
© Springer-Verlag 2007

**Abstract** In this paper we present a mechanical model that intends to capture the kinematical aspects of thrust fault related folds induced by regional-scale far-field contraction. Fold shapes may be the only surface evidence of the geometry of underlying faults, so complex fault interactions are assessed in terms of how they influence fold geometry. We use the finite element method to model the fold and finite deformation frictional contact to model the activation and evolution of slip throughout preexisting faults. From several simulated 2D fault patterns we infer how one may form an anticline similar to that observed at Sheep Mountain Anticline, Wyoming.

**Keywords** Anticline · Finite element · Fold · Frictional contact · Rock · Thrust fault

## 1 Introduction

Mechanical models that follow the evolution of stresses and deformation are essential for understanding the origin of folding and the sequence of faulting in a fold and thrust mountain belt. Thrust faults commonly are associated with folds that grow in amplitude as underlying faults slip [6, 22, 64, 77, 78, 84]. Fold patterns may be the only surface evidence of the geometry of underlying faults [67, 68, 71, 74], so advances in the study of fault

mechanisms and how they influence fold geometry can assist in our interpretation not only of the process and sequence of faulting but also of the origin and probable stress distributions in folds.

Faults are narrow zones within Earth's crust where shear strains are intense and where slip is dominated primarily by friction. Experimental and theoretical investigations of the frictional properties of fault surfaces have shown that the coefficient of friction depends on slip velocity, maturity of contact, rock-mass stiffness, and temperature [14, 28, 66, 69, 88]. For most quasi-static applications such variation of the coefficient of friction is not as significant as that encountered in dynamic rupture propagation, where sliding velocities are much faster than those commonly encountered in laboratory experiments. Dynamic processes can activate additional weakening mechanisms such as flash heating, resulting in a much lower coefficient of friction [49, 62].

A challenging aspect of thrust faulting as it affects fold geometry lies in the mathematical capture of the intense shear strain concentrated over a very narrow zone. In the context of finite element (FE) analysis, there are many alternative approaches that one can possibly pursue to model thrust faulting, including: (a) the embedded discontinuity approach [9, 11, 15, 16]; (b) the extended finite element approach, or XFEM [29, 40, 57]; and (c) the contact mechanics technique [5, 20, 31, 44, 58, 73, 93]. All of these approaches entail some form of regularization to characterize the thickness of the fault. A convenient regularization is to assume that the fault thickness is zero, which gives rise to a discontinuous velocity field. Techniques (a) and (b) allow the fault to pass through a finite element and "slice" it; they are typically used to simulate fault rupture and fault propagation. A shortcoming of these methods is that they only can

---

P. F. Sanz · R. I. Borja (✉)  
Department of Civil and Environmental Engineering,  
Stanford University, Stanford, CA 94305, USA  
e-mail: borja@stanford.edu

D. D. Pollard  
Department of Geological and Environmental Sciences,  
Stanford University, Stanford, CA 94305, USA

accommodate small slips. Technique (c) can accommodate very large slips; however, it has a disadvantage in that the geometry of the fault must be predefined. Thrust faulting has also been modeled with the finite difference approach [32, 63, 82], the distinct element method, or DEM [21, 34, 43, 83], and the boundary element method, or BEM [6, 24, 68].

Stresses that arise in strata during fold development are unlikely to be explained by one faulting mechanism [42]. For example, strata that are domed by an expanding magma chamber experience considerable stretching, which is not included in bending models [46]. The interaction between deforming layers with different constitutive properties is known to affect the local stress field [3, 4, 18, 54, 87], as does the interfacial conditions of the layer boundaries [23, 24, 48]. The stress distribution changes over time as the fault slips, the fold evolves, and the bedding rotates [30, 38]. Early formed opening fractures may rotate and be activated in shear, thus affecting the stress distribution [7, 26, 27, 89]. Given the above complexities it is no wonder that progress has been slow in developing models for fault-related folding processes.

Current advances in computational techniques have allowed the development of more realistic mechanical models for characterizing faulting and fold evolution with time. There have been several kinematical models that attempt to unravel faulting and fold evolution with time using both backward and forward modeling, calibrated with respect to the present-day shape of the fold (e.g. [19, 25, 33, 47, 56, 85]). Our approach is to pursue a forward modeling to follow the deformation, assuming an initial configuration and imposing boundary conditions and initial imperfections. Mechanical modeling only requires far-field boundary conditions and a solution method for the governing equations of motion to calculate the stresses and deformation in the fold. Hence, the solution not only provides a great deal of understanding of the kinematic puzzle, it also satisfies the laws of physics for a continuum body undergoing a quasi-static deformation process. As opposed to kinematic and geometric models, our mechanical model solutions satisfy the equilibrium differential equations, the compatibility conditions for the kinematics, along with phenomenological stress-strain relations for the rock layers. These latter attributes are useful particularly for understanding the sequence of faulting in the fold [6, 7, 37, 68, 70]. In addition, forward mechanical modeling is useful for checking the validity of several crucial kinematical assumptions such as hinge migration [1, 8, 84], fixed hinge [33, 55, 75], rotating limbs [33], or fixed limb dip [84, 86].

In this paper we use the FE method along with finite deformation frictional contact mechanics to model

large-scale thrust faulting and regional-scale folding of geologic strata. This work addresses the reactivation of existing faults subjected to new tectonic events and not the initiation of faults. Hence, the geometry of the fault in our analysis is known a priori. Forward modeling is formulated by a Lagrangian description of nonlinear continuum mechanics [52, 60], in which any point in the current configuration is mapped with a material point in a reference configuration. As the layers fold their geometry changes and the directions of the principal stress axes rotate. Faults are structural features that translate and rotate with the deforming domain; their motions are also tracked by the Lagrangian formulation [10, 11]. Compared to kilometer-scale folding the fault thickness is very small, so in this paper we assume that the fault thickness is zero [2, 13].

Because the mechanical response is influenced by a large number of variables, including the fault geometry, material parameters, and the boundary conditions, we have performed a number of preliminary simulations and observed the following variables to exhibit direct and significant effects on deformation and fault movement: fault dip, fault depth, fault length, and coefficient of friction. The first three variables are structural features, whereas the fourth is a material parameter. The ductility of the rock above the fault is another material property that dictates whether the top layer would fold or fault. In this paper we assume that the overlying rock has sufficient ductility so that it would simply fold when deformed by a fault. We show that slip on an inclined fault generates an asymmetric anticline, and that the degree of asymmetry is a function of the fault dip and fault depth. We also show that the forelimb side of an asymmetric anticline experiences the greatest amount of stretching and distortion and therefore is most susceptible to fracturing, deformation banding, cataclasis, and other forms of material damage.

## 2 Mathematical description of a fault

In this section we describe the important mathematical elements of a fault. The framework is quite robust in that it formulates the problem in 3D for any quasi-static loading condition and for any displacement and traction boundary conditions.

### 2.1 Kinematics: fold deformation and fault orientation

We assume a reference configuration  $\mathcal{B}$  for a body that may contain faults and deform by folding, and denote any material point in this configuration by  $X$ . We can take  $\mathcal{B}$  as the initial unfaulted and unfolded configuration or any

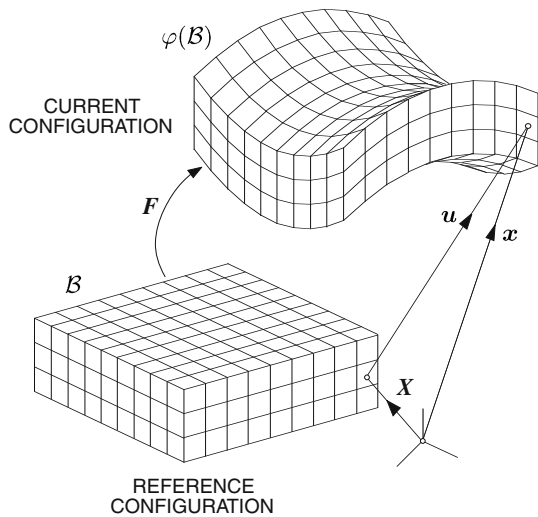


**Fig. 1** Reference and current configurations of a fold. Note: reference configuration is not necessarily undeformed

updated configuration, see Fig. 1. Let us construct a Cartesian coordinate reference frame and denote the initial coordinates of  $X$  by  $\mathbf{X}$ . After some deformation,  $\mathcal{B}$  would have moved to its current configuration  $\varphi(\mathcal{B})$  so that the material point  $X$  now has Cartesian coordinates  $\mathbf{x}$ . If  $\mathbf{u}$  is the displacement of  $X$ , then

$$\mathbf{x} = \mathbf{X} + \mathbf{u}. \tag{1}$$

We recall the deformation gradient  $\mathbf{F} = \partial \mathbf{x} / \partial \mathbf{X}$ , and its polar decomposition

$$\mathbf{F} = \mathbf{R} \cdot \mathbf{U} = \mathbf{V} \cdot \mathbf{R}, \tag{2}$$

where  $\mathbf{R}$  is a proper orthogonal tensor, and  $\mathbf{U}$  and  $\mathbf{V}$  are the symmetric right and left stretch tensors, respectively. The deformation gradient  $\mathbf{F}$  plays a central role in defining different measures of stresses and deformation in a non-linear continuum.

The Jacobian determinant  $J$  is given by the expression

$$J = \det(\mathbf{F}) = \frac{\rho_0}{\rho} = \frac{dv}{dV}, \tag{3}$$

where  $(\rho, dv)$  and  $(\rho_0, dV)$  are the mass density and differential volume in the current and reference configurations, respectively. Note that the law of conservation of mass states that  $\rho dv = \rho_0 dV$ , so  $J$  describes how much the elementary reference volume  $dV$  has contracted ( $J < 1$ ) or expanded ( $J > 1$ ). Rocks experiencing plastic flow can either compact or dilate depending on their initial porosity, and this volume behavior is reflected by the evolution of  $J$ .

Next we describe the kinematics of a fault. A fault is a structural element that moves with deformation. For

example, if a domain contains a fault and rotates as a rigid body, then the fault moves with the domain and rotates by the same amount. It is convenient to define the orientation of a fault by a unit normal vector  $\mathbf{N}$  to the elementary surface area  $dA \in \mathcal{S}$ , where  $\mathcal{S} \in \mathcal{B}$  is the surface of the fault reckoned with respect to the reference configuration  $\mathcal{B}$ . Because  $\mathcal{B}$  is fixed,  $\mathbf{N}$  is invariant with time. However, the current configuration  $\varphi(\mathcal{B})$ , also called the ‘‘push-forward’’ of  $\mathcal{B}$ , evolves with deformation. Let  $da$  and  $\mathbf{n}$  denote the push-forwards of  $dA$  and  $\mathbf{N}$ , respectively, and assume that  $\mathbf{n}$  remains a unit vector to  $da \in \varphi(\mathcal{S})$ . Then Nanson’s formula [60] states that

$$\mathbf{n} da = J \mathbf{F}^{-t} \cdot \mathbf{N} dA, \tag{4}$$

where  $\mathbf{F}$  is interpreted as the deformation gradient of an infinitesimal volume  $dV$  containing the elementary area  $dA$ . If there is no stretching involved, then  $\mathbf{U} = \mathbf{V} = \mathbf{I}$ , and so  $\mathbf{F} = \mathbf{R}$ ,  $J = 1$ , and  $da = dA$ . In this case  $dA$  simply rotates as a rigid body by an amount determined by the proper orthogonal tensor  $\mathbf{R}$ , see Fig. 2.

Let us assume that the fault has reference and current thicknesses  $h_0$  and  $h$ , respectively. We assume here that the thicknesses  $h$  and  $h_0$  are so small that we can take the elementary volume in the reference configuration as  $dV = h_0 dA$  and its push-forward as  $dV = h da$ . The Jacobian determinant then becomes  $J = (h da) / (h_0 dA)$ , and Nanson’s formula reduces to

$$\mathbf{n} = \frac{h}{h_0} \mathbf{F}^{-t} \cdot \mathbf{N} \equiv \frac{h}{h_0} \mathbf{N} \cdot \mathbf{F}^{-1}. \tag{5}$$

Borja [10] used the above equation to describe the evolving orientation of a deformation band in the regime of large deformation.

### 2.2 Slip on a fault

We define the instantaneous velocity field of any material point  $X \in \mathcal{B}$  inside a fault by the ramp-like relation

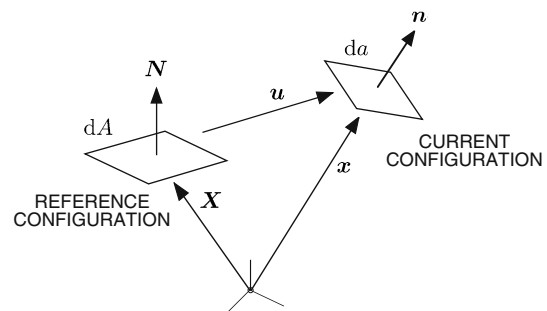


**Fig. 2** Differential areas and unit normal vector on a fault surface in the reference and current configurations

$$\mathbf{v}(X) = \begin{cases} \bar{\mathbf{v}} & \text{if } \kappa \leq 0; \\ \bar{\mathbf{v}} + \kappa \llbracket \mathbf{v} \rrbracket / h_0 & \text{if } 0 \leq \kappa \leq h_0; \\ \bar{\mathbf{v}} + \llbracket \mathbf{v} \rrbracket & \text{if } \kappa \geq h_0, \end{cases} \quad (6)$$

where  $\bar{\mathbf{v}}$  is a continuous velocity field,  $\llbracket \mathbf{v} \rrbracket$  is the relative velocity of two opposite faces of the fault, and  $\kappa \in [0, h_0]$  is the normal coordinate to the fault in the reference configuration. We assume that  $h_0$  is so small that the two opposite fault faces in the neighborhood of  $X$  may be considered parallel.

Let  $\dot{\mathbf{F}} = \partial \mathbf{v} / \partial X$  denote the material time derivative of the deformation gradient inside the fault. From Eq. 6, we get

$$\dot{\mathbf{F}}(X) = \dot{\bar{\mathbf{F}}} + (\llbracket \mathbf{v} \rrbracket \otimes \mathbf{N}) / h_0 \quad \text{if } 0 \leq \kappa \leq h_0, \quad (7)$$

where

$$\dot{\bar{\mathbf{F}}} = \frac{\partial \bar{\mathbf{v}}}{\partial X} + \frac{\kappa}{h_0} \frac{\partial \llbracket \mathbf{v} \rrbracket}{\partial X}. \quad (8)$$

The derivative  $\partial \llbracket \mathbf{v} \rrbracket / \partial X$  represents the spatial variation of the velocity jump on the fault; since  $0 \leq \kappa / h_0 \leq 1$ , this derivative and the gradient of the continuous velocity field  $\partial \bar{\mathbf{v}} / \partial X$  are bounded. The intense deformation gradient inside the fault is

$$\llbracket \dot{\mathbf{F}} \rrbracket = \frac{\dot{\zeta}}{h_0} \mathbf{m} \otimes \mathbf{N}, \quad (9)$$

which is typically orders of magnitude greater than  $\dot{\bar{\mathbf{F}}}$  since  $h_0 \approx 0$ . In the above equation we have written the velocity jump as  $\llbracket \mathbf{v} \rrbracket = \dot{\zeta} \mathbf{m}$ , where  $\dot{\zeta}$  is the magnitude of the velocity jump and  $\mathbf{m}$  is the unit vector in the direction of this jump.

Let  $\mathbf{l} = \partial \mathbf{v} / \partial \mathbf{x}$  denote the velocity gradient and recall that  $\mathbf{l} = \dot{\mathbf{F}} \cdot \mathbf{F}^{-1}$ . Then the jump of  $\mathbf{l}$  inside the fault is obtained by post-multiplying Eq. 9 with  $\mathbf{F}^{-1}$  and using Eq. 5 to get

$$\llbracket \mathbf{l} \rrbracket = \llbracket \dot{\mathbf{F}} \rrbracket \cdot \mathbf{F}^{-1} = \frac{1}{h} \llbracket \mathbf{v} \rrbracket \otimes \mathbf{n} = \frac{\dot{\zeta}}{h} \mathbf{m} \otimes \mathbf{n}. \quad (10)$$

Accordingly, the jump in the rate of deformation is the symmetric part of  $\llbracket \mathbf{l} \rrbracket$ ,

$$\llbracket \mathbf{d} \rrbracket = \text{sym}(\llbracket \mathbf{l} \rrbracket) = \frac{\dot{\zeta}}{h} \text{sym}(\mathbf{m} \otimes \mathbf{n}). \quad (11)$$

Note that both  $\llbracket \mathbf{l} \rrbracket$  and  $\llbracket \mathbf{d} \rrbracket$  are second-order tensors of rank one, i.e., they both have exactly one non-zero eigenvalue. A pure tangential slip is characterized by the condition

$$\mathbf{m} \cdot \mathbf{n} = 0 \quad \implies \quad \text{tr}(\llbracket \mathbf{l} \rrbracket) = \text{tr}(\llbracket \mathbf{d} \rrbracket) = 0, \quad (12)$$

which is what we will try to capture with the contact algorithm described in the next section.

In the limit of zero thickness the fault becomes a ‘‘crack’’ and the ramp function given by Eq. 6 becomes a Heaviside function. In this case the jump in the rate of deformation reduces to a distribution function of the form

$$\llbracket \mathbf{d} \rrbracket = \delta_S \text{sym}(\dot{\zeta} \mathbf{m} \otimes \mathbf{n}), \quad (13)$$

where  $\delta_S$  is the Dirac delta function. The assumption of a zero fault thickness is a mathematical convenience that is widely used in modeling strong discontinuity kinematics [9, 11, 16, 61]. We shall take this assumption along with the condition for pure tangential sliding to formulate the general 3D constitutive model for frictional contact described below.

### 2.3 Frictional contact on a fault

For a fault deforming by tangential frictional sliding we consider the classical Mohr–Coulomb friction law formulated in the Lagrangian description. Following Laursen and Simo [50], we take the nominal traction vector at material point  $X$  on the fault as  $\mathbf{t} = \mathbf{P} \cdot \mathbf{N}$ , where  $\mathbf{P}$  is the non-symmetric first Piola–Kirchhoff stress tensor defining the total force in the current configuration acting per unit surface area in the undeformed configuration, and  $\mathbf{N}$  is the same unit normal vector to the fault defined previously. We can resolve this traction into normal and tangential components at the current configuration as

$$\mathbf{t}(X, t) = t_N(X, t) \mathbf{n} + t_T(X, t) \boldsymbol{\xi}, \quad (14)$$

where  $t_N$  and  $t_T$  are normal and tangential components of the nominal traction vector obtained from

$$t_N = \mathbf{n} \cdot \mathbf{P} \cdot \mathbf{N}, \quad t_T = \|\mathbf{t}_T\|, \quad \boldsymbol{\xi} = \mathbf{t}_T / t_T, \quad \mathbf{t}_T = \mathbf{t} - t_N \mathbf{n}. \quad (15)$$

Note that  $t_N$  (negative for compression) and  $t_T$  are resolved nominal stresses representing forces in the current configuration per unit undeformed area.

Next we write the Mohr–Coulomb friction law at residual state using the format of classical plasticity. Let  $\mu$  denote the coefficient of friction; then we have

$$\Phi = t_T + \mu t_N \leq 0, \quad \llbracket \mathbf{v} \rrbracket = \dot{\zeta} \boldsymbol{\xi}, \quad \dot{\zeta} \geq 0, \quad \Phi \dot{\zeta} = 0. \quad (16)$$

In the above expressions  $\Phi$  takes the role of the yield function at residual state,  $\llbracket \mathbf{v} \rrbracket$  is the velocity jump across the fault (evaluated from a non-associative flow rule),  $\dot{\zeta}$  is the nonnegative slip rate, and the fourth expression is the Kuhn–Tucker condition. The fault kinematics yields  $\llbracket \dot{\mathbf{J}} \rrbracket = \mathbf{J} \text{tr} \llbracket \mathbf{l} \rrbracket = 0$ , since  $\mathbf{m} \cdot \mathbf{n} = 0$  for a fault that moves by

pure tangential sliding. Furthermore, the flow rule suggests that the velocity jump  $[[\mathbf{v}]]$  across the fault is fully plastic, consistent with results obtained for strong discontinuity kinematics by Borja [9, 10], among others.

#### 2.4 Large deformation frictional contact model

In this work we capture the kinematics and frictional response of faulting using a frictional contact model for large deformations. Our numerical implementation includes three types of nonlinearities: material, geometric, and contact constraints along the fault. We model the mechanical response along the fault using Coulomb's friction law. This constitutive law does not provide a unique value of the tangential traction when the displacement jump across the fault is zero. To avoid this possibility, our implementation considers a regularized Coulomb friction law. Thus we can formulate the constitutive equation within the framework of elasto-plasticity, splitting the tangential velocity jump  $[[\mathbf{v}]]$  into elastic (stick)  $[[\mathbf{v}^e]]$  and plastic (slip) parts  $[[\mathbf{v}^p]]$  as

$$[[\mathbf{v}]] = [[\mathbf{v}^e]] + [[\mathbf{v}^p]]. \quad (17)$$

The model considers the stick response as linearly elastic. The time derivative of the tangential contact traction  $\dot{\mathbf{t}}_T$  is given by

$$\dot{\mathbf{t}}_T = \epsilon_T ([[ \mathbf{v} ] - [[ \mathbf{v}^p ]]), \quad (18)$$

where  $\epsilon_T$  is a regularization parameter that may be thought of as a tangential elastic constant. Similar to Eq. 16, we state the flow rule as

$$[[\mathbf{v}^p]] = \zeta \boldsymbol{\xi}. \quad (19)$$

Note that the above equation does not predict the total offset across the fault but only the plastic component. This frictional flow rule is path-dependent and requires the integration of the constitutive law. The local integration is performed by a return mapping algorithm [50, 92]) in a similar way to a non-associative plasticity model.

A critical aspect of the numerical implementation is the choice of method to convert the variational inequality of a contact constraint into an equality suitable for finite element implementation. Most proposed techniques use either the penalty method or the method of Lagrange multipliers. The penalty method has the particular benefit of eliminating the constraints explicitly from the variational formulation, and when addressing the frictional problem this feature offers distinct advantages [50]. Our implementation applies the penalty method to impose the normal

constraints. In this formulation, the normal component of the contact force  $t_N$  is directly proportional to the normal penetration of a contact node into the contact surface encountered. This penetration (gap)  $g_N$  is defined via a minimum distance function between the spatial configuration of the contacting surfaces [50, 72]. When  $g_N < 0$ , contact occurs and the normal component of the contact traction is

$$t_N = \mathbf{t} \cdot \mathbf{n} = \epsilon_N g_N < 0, \quad (20)$$

where  $\epsilon_N$  is a penalty parameter that penalizes the penetration in the normal direction. It can be shown [51] that the impenetrability condition (Lagrange multipliers solution) is recovered from this formulation when  $\epsilon_N \rightarrow \infty$ ; however, very large values of  $\epsilon_N$  could lead to an ill-conditioned system. A simple estimate of a recommended upper bound of the penalty parameter can be found in Nour-Omid and Wriggers [59].

For the finite element implementation our point of departure is the variational form of the linear momentum balance, written with respect to the reference configuration as

$$\int_B (\text{GRAD} \boldsymbol{\eta} : \mathbf{P} - \rho_0 \boldsymbol{\eta} \cdot \mathbf{G}) dV - \int_{\partial \mathcal{B}_\sigma} \boldsymbol{\eta} \cdot \mathbf{t}_0 dA - \int_{\partial \mathcal{B}_c} \boldsymbol{\eta} \cdot \mathbf{t} dA = 0, \quad (21)$$

where  $\boldsymbol{\eta}$  is the weighting function,  $\rho_0$  is the mass density in the reference configuration,  $\mathbf{G}$  is the vector of gravity accelerations,  $\mathbf{t}_0$  is the nominal traction vector acting on the traction boundary  $\partial \mathcal{B}_\sigma$ , and  $\mathbf{t}$  is the nominal traction vector acting on the contact surface  $\partial \mathcal{B}_c$ . The gradient operator GRAD is a spatial differentiation with respect to the coordinates of the reference configuration and  $B$  is the union of the contacting domains in the reference configuration. Note that the last term of Eq. 21 corresponds to the virtual work by the contact forces  $\mathcal{W}^c$ , which is defined according to

$$\mathcal{W}^c = - \int_{\partial \mathcal{B}_c} [t_N \eta_N + t_T \eta_T] dA, \quad (22)$$

where  $\eta_N$  and  $\eta_T$  are the variations of the gap and slip respectively. In order to integrate Eq. 22 we discretize the contact surface  $\partial \mathcal{B}_c$  into node-to-segment finite elements. Herein, we use the so-called slave-master concept for the contacting surfaces. We assume that one of the contacting surfaces is the slave and its nodes are called slave nodes. The other contacting surface, the master, is divided into master segments that span master nodes. In our model, a slave node can make contact with only one master

segment, but one master segment may contact with one or more slave nodes at the same time. This formulation allows for a slave node to slide over the entire contact (master) area. For this reason we perform a search algorithm of the contacts at each Newton–Raphson iteration to check and update the contact element connectivity if required. A detailed discussion of the node-to-segment contact element can be found in Wriggers [90, 91]. The implementation of our model includes a consistent linearization of Eq. 21 to enable optimal convergence for Newton–Raphson iterations, essential for the general robustness of implicit finite element techniques.

### 3 Simulation of generic problems

We have implemented the mechanical model in a Fortran nonlinear finite element code based on a fully Lagrangian description with an algorithm for finite deformation frictional contact. Results reported in this section pertain to 2D plane strain conditions employing hyperelastic constant strain triangular elements and node-to-segment frictional contacts sliding according to the Mohr–Coulomb law. We use a penalty formulation to prevent interpenetration of node-to-segment contacts; gapping is allowed where the contact elements tend to separate. Iterations for nonlinearities induced by finite deformation effects and node-to-segment frictional contacts are carried out by a full Newton–Raphson iterative scheme with a convergence error tolerance of  $10^{-6}$  based on the norm of the initial residual force vector.

#### 3.1 Problem definition

The overall geometry of a generic problem is shown in Fig. 3. A rectangular domain 120 km wide and 60 km deep is shortened horizontally from the left vertical side by a

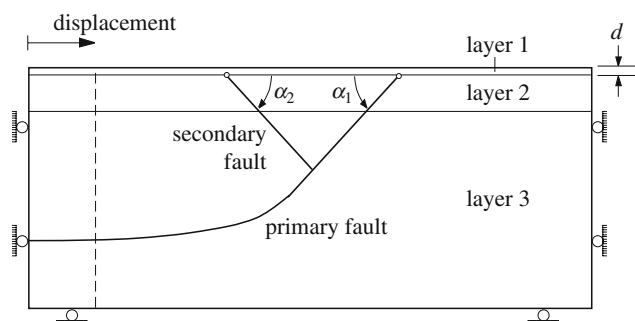


**Fig. 3** Problem definition for primary and secondary thrust faults at depth  $d$  subjected to horizontal contraction, with initial dips  $\alpha_1$  and  $\alpha_2$ , respectively

prescribed uniform displacement. Frictional sliding is allowed on a predefined primary thrust fault. In the following simulations we focus on investigating the effects of different fault geometries on the slip distribution and the resulting surface fold shapes. Because of the kinematical limitations of a 2D plane strain configuration, the deformation is restricted to in-plane faulting. We assume that the underlying primary fault is well defined, with near-surface dip  $\alpha_1$  and curving to a horizontal orientation at a prescribed depth. We can place the fault tip either at the upper traction free surface or at some distance  $d$  below it; here we choose the latter since this produces a fold rather than a break on the model Earth’s surface. This is consistent with the geological observations for an anticline at Sheep Mountain (Sect. 4).

To understand the mechanics of fault interaction on this generic configuration, we also consider a secondary (shorter) fault with initial dip  $\alpha_2$  and terminating at the intersection with the primary fault with a geometry similar to back thrusts. We assume a Young’s modulus that increases with depth:  $E = 5$  GPa for the layer above the fault tip, 10 GPa for the next 4 km, and 20 GPa for the bottom 55 km (layers 1, 2, and 3, respectively); and a Poisson’s ratio  $\nu = 0.25$  for all three layers. Weight per unit volume for all rocks is  $26 \text{ kN/m}^3$ , which was applied as a downward body force prior to applying the horizontal contraction (the body force generates a significant component of frictional resistance along the fault).

In addition to the surface fold shape, we are also interested in calculating the slip distribution along the primary and secondary faults as a result of the imposed horizontal contraction. Domains are always finite in the context of finite element analysis, so in the present analysis we shall assume that the two vertical boundaries in Fig. 3 are sufficiently distant from the fault tip to represent conditions in the “far-field”. That the primary fault curves horizontally at depth and intersects the left vertical boundary where there is no slip suggests that a zero “far-field” slip is captured by the mechanical model only in an approximate sense. We assume a quasi-static condition and calculate the deformation from an elliptic partial differential equation ignoring inertia effects. This implies that any imposed boundary motion is felt instantaneously by the entire domain. Depending on the fault geometry and friction coefficient, the Mohr–Coulomb slip condition may be violated at some critical points on the fault causing slip to initiate at those points; we also aim to identify regions on the fault where slip is likely to initiate. We emphasize that throughout this paper we specify the fault geometry beforehand and that there is no nucleation of a new fault or propagation of old faults. The subject of fault nucleation/growth is beyond the scope of this paper and will be addressed in future work.

### 3.2 Isolated thrust fault

In this series of simulations we suppress the secondary fault and only consider the primary fault. In general, the calculated mechanical response is influenced by a large number of variables, and in order to limit the number of simulations we shall only consider the following variables that we observed to have shown significant influence on the calculated slip magnitudes and fold shape: initial dip  $\alpha_1$ , coefficient of friction  $\mu$ , and fault depth  $d$ . It is important to note that  $\alpha_1$  increases with horizontal contraction as the domain becomes narrower and deeper. The mechanical model automatically calculates this nonlinear geometric evolution of  $\alpha_1$  throughout the simulation.

Figures 4 and 5 show the deformed finite element meshes after a horizontal contraction of 10 and 13 km (8.3 and 10.8% nominal horizontal strain) assuming  $\alpha_1 = 35^\circ$  and  $\mu = 0.577$ , and taking  $d = 1$  and 2 km depth, respectively. In both cases the fault initially slips at the tip and the disturbance propagates downwards until it “dissipates” at the left vertical boundary. As slip continues the fault tip experiences an opening and the contact elements separate, forming a gap. This kinematical feature is required to allow layer #1 to fold without faulting as slip accumulates near the fault tip. Figures 6 and 7 show snapshots of deformation near the fault tip and reveal that some continuum elements rotate and stretch to allow slip near the fault tip without faulting the overlying ductile layer. The controlling variable (independent parameter) in these figures is the nominal horizontal strain  $\varepsilon$  representing the ratio of the imposed horizontal displacement to initial domain width of 120 km (see Fig. 3).

The displacements shown in Figs. 6 and 7 are true, i.e., they have not been magnified. The gap forming near the

fault tip may in reality be filled with fragmented rocks of a fault damage zone. Unfortunately, the standard finite element method cannot capture these smaller-scale damage processes occurring around the fault tip; nevertheless, it still is useful for interpreting deformations occurring at the fold scale.

Thrust faulting in the subsurface creates an asymmetric anticline. We see in Figs. 6 and 7 that at the same  $\varepsilon$  the curvature at the hinge of the anticline is sharper for the shallower fault ( $d = 1$  km) than for the deeper fault ( $d = 2$  km), and the asymmetry also is stronger. Regardless of depth  $d$ , the distortion and stretching of the elements on the forelimb side are seen to be more pervasive than those on the backlimb side, so we can expect damage in the form of fractures, deformation bands, cataclastic flow, etc. to be denser on the forelimb than on the backlimb of an asymmetric anticline [35].

In Fig. 8 we reduce the coefficient of friction  $\mu$  to 0.268 thereby making it easier for the fault to slip. Comparing with Fig. 6, we see that the anticline reaches a similar amplitude and asymmetry at lesser values of imposed strain  $\varepsilon$ . In Fig. 9 we increase the dip  $\alpha_1$  to  $45^\circ$  and compare the fold shapes to those of Fig. 8. We see that fold amplitude and asymmetry are less for the same  $\varepsilon$  and, therefore, it takes more horizontal contraction to achieve a comparable fold shape. Furthermore, the greater the dip the less asymmetric the anticline. We emphasize that the snapshots shown in Figs. 6, 7, 8 and 9 also show true relative elevations from frame #1 to frame #3 in that as the top layer folds both sides of the anticline rise in elevation due to Poisson’s ratio effect.

Figures 10 and 11 show the calculated evolutions of maximum fault slip  $\zeta$ , occurring near the fault tip, and structural relief  $h$ , the vertical distance from the highest

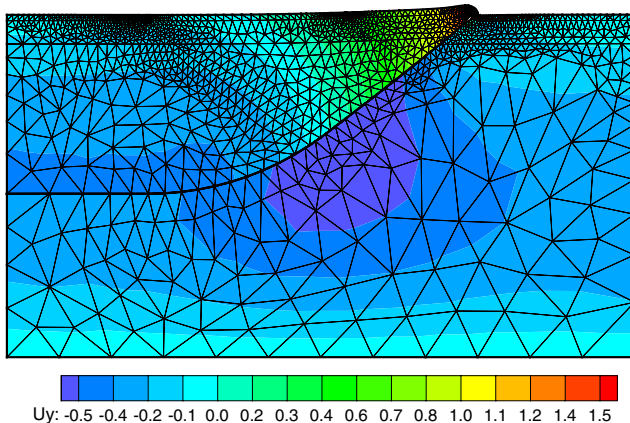


**Fig. 4** Deformed mesh for an isolated fault 1 km deep after a horizontal contraction of 10 km. Initial dip  $\alpha_1 = 35^\circ$ ; coefficient of friction on the fault  $\mu = 0.577$ ; vertical displacement bar in kilometer

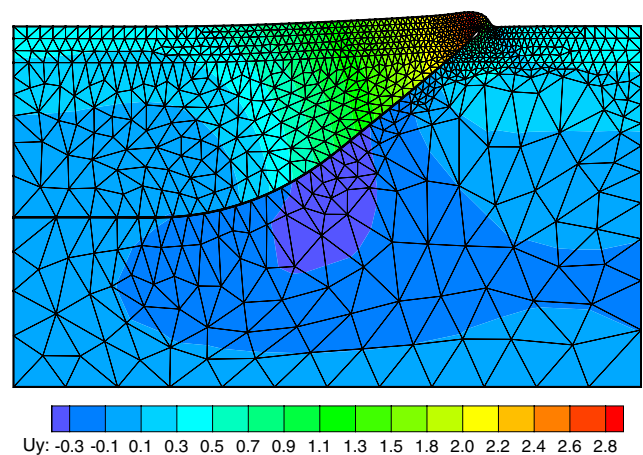


**Fig. 5** Deformed mesh for an isolated fault 2 km deep after a horizontal contraction of 13 km. Initial dip  $\alpha_1 = 35^\circ$ ; coefficient of friction on the fault  $\mu = 0.577$ ; vertical displacement bar in kilometer

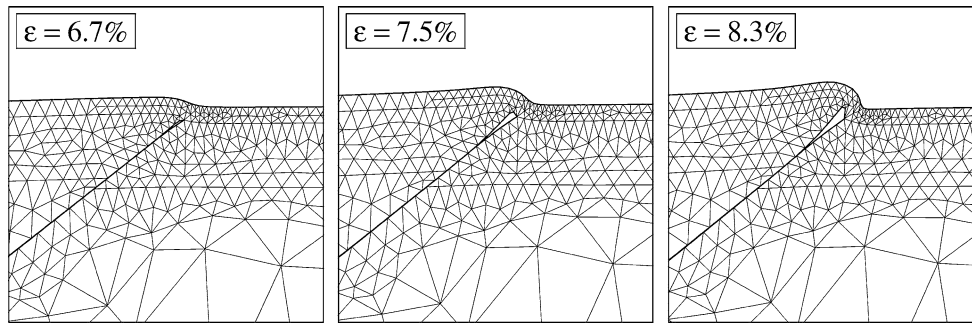


**Fig. 6** Snapshots of deformation around the fault tip for an isolated fault with  $\alpha_1 = 35^\circ$ ,  $\mu = 0.577$ , and  $d = 1$  km. Controlling variable  $\varepsilon$  is the nominal horizontal strain

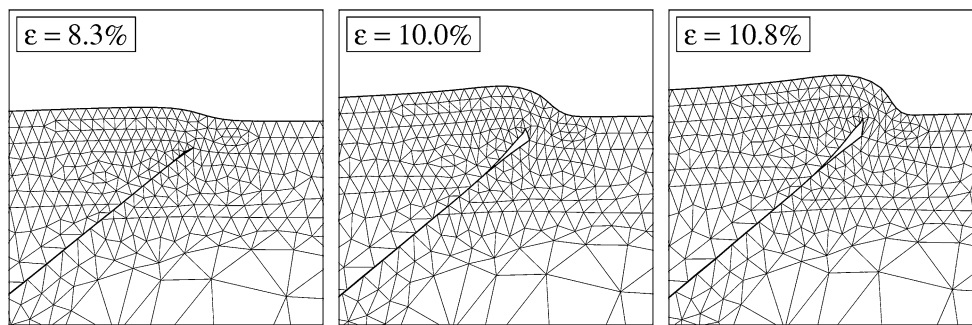


**Fig. 7** Snapshots of deformation around the fault tip for an isolated fault with  $\alpha_1 = 35^\circ$ ,  $\mu = 0.577$ , and  $d = 2$  km

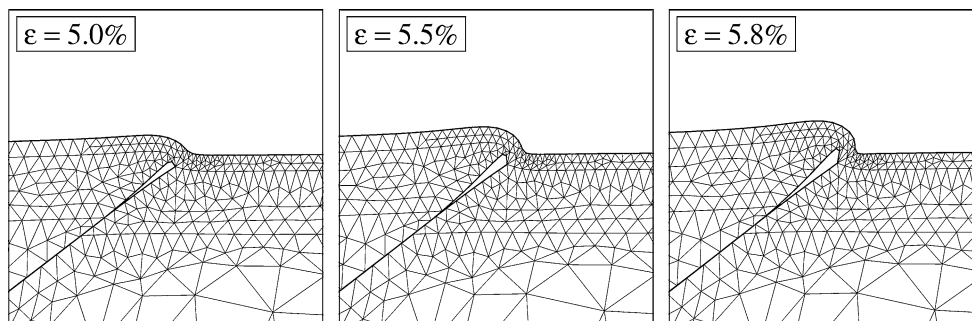


**Fig. 8** Snapshots of deformation around the fault tip for an isolated fault with  $\alpha_1 = 35^\circ$ ,  $\mu = 0.268$ , and  $d = 1$  km

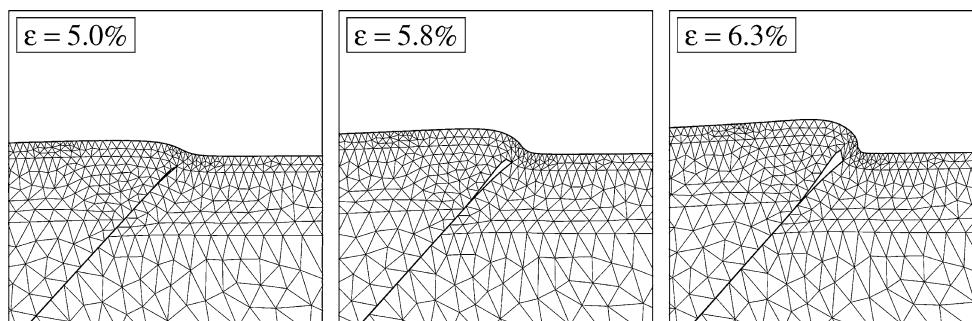


**Fig. 9** Snapshots of deformation around the fault tip for an isolated fault with  $\alpha_1 = 45^\circ$ ,  $\mu = 0.268$ , and  $d = 1$  km

point of the fold to the foot of the anticline on the forelimb side. Calculated slips are greater for the shallower fault (Fig. 10) than for the deeper fault (Fig. 11), as expected. Calculated slips also are greater for the weaker fault ( $\mu = 0.268$ ) than for the stronger fault ( $\mu = 0.577$ ), also as expected.

If the sliding wedge of material above the inclined portion of the thrust fault were rigid and the fault tip was near the ground surface, then the relation between  $\zeta$  and  $h$  would be  $h = \zeta \sin \alpha_1$ . Figures 10 and 11 indeed show that  $h/\zeta \approx 0.57$  during the early stage of slipping when  $\alpha_1 \approx 35^\circ$ . However, as the mesh is compressed  $\alpha_1$  increases in a nonlinear way, and the ratio  $h/\zeta$  likewise increases above the value 0.57. On the other hand, for  $d = 1$  km Fig. 10 shows that the ratio  $h/\zeta$  later decreases as the tip of the fault “bends” and the hinge of the anticline “migrates”. This is partially due to the high tensile resistance developed by the finite elements on the forelimb side, which were assumed to be very ductile. This also would be changed if bedding-plane slip were allowed within layer #1, a phenomenon observed in some locations on Sheep Mountain Anticline (Sect. 4). Evidently, a more realistic modeling would entail simulation of the degradation of strength and eventual tensile fracturing of these finite elements as well as slip between layers.

### 3.3 Interaction with a shorter fault

In the following series of simulations we activate the secondary fault (a back thrust) to investigate the influence of this shorter fault on fold shape and slip. The examples are

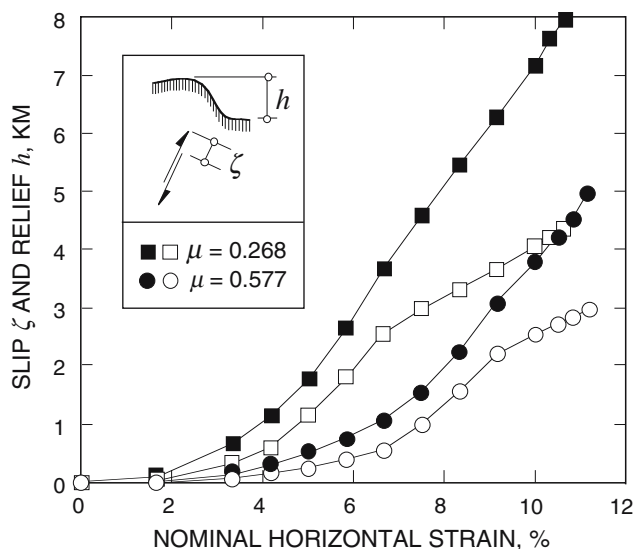


**Fig. 10** Geometrical evolution of surface fold as a function of imposed horizontal contraction for  $\alpha_1 = 35^\circ$  and  $d = 1$  km. Dark symbols denote maximum slip, open symbols denote structural relief

not meant to represent any specific field condition, they simply show some general trends that could be useful in understanding deformation processes as well as in interpreting fold geometries arising from more complex fault patterns.

In Fig. 12 we shorten the finite element mesh horizontally by 10.4 km (or 8.7% nominal horizontal strain), assuming  $\alpha_1 = \alpha_2 = 35^\circ$  and  $d = 1$  km. The prescribed contraction is significant enough to produce a pair of distinct anticlines, but small enough that the dips of the two forelimbs remain less than  $90^\circ$ . The two anticlines are comparable in height, although the structural relief produced by the secondary fault is less since this fault is shorter and therefore cannot develop as much slip as can the longer fault. The wedge produced by the two faults is colored red-to-green in Fig. 12 and indicates that it has been pushed upwards by the converging vertical boundaries. If the faults were 2 km deep, Fig. 13 suggests that the horizontal contraction would have to be as large as 13.6 km (or 10.5% nominal strain) in order to develop a similar surface fold shape.

Figure 14 shows slip intensities along the fault axes, where the normal distance of the point from the fault represents the magnitude of the accumulated tangential slip on that fault. Note that the tangential slip on the secondary fault is less than in the primary fault even though the two faults have the same dip. This is because the primary fault is longer and therefore can develop greater slip. Also, note that for any given contraction  $\varepsilon$  the maximum slip occurs near the fault tip. Slip rapidly approaches zero at the fault tip since the fault is not allowed

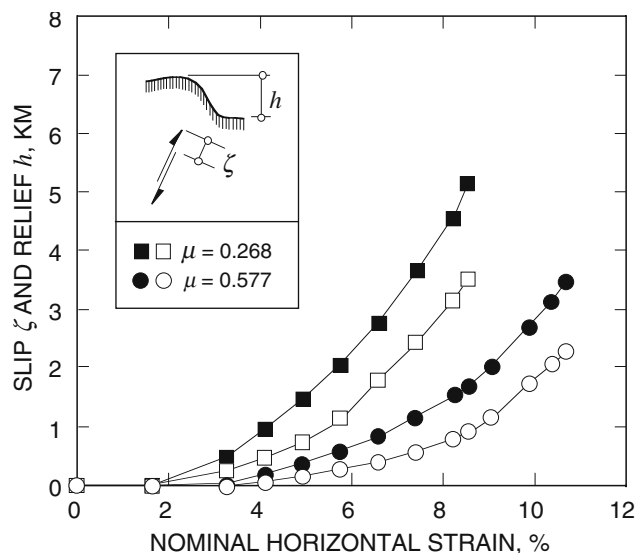


**Fig. 11** Geometrical evolution of surface fold as a function of imposed horizontal contraction for  $\alpha_1 = 35^\circ$  and  $d = 2$  km. Dark symbols denote maximum slip, open symbols denote structural relief

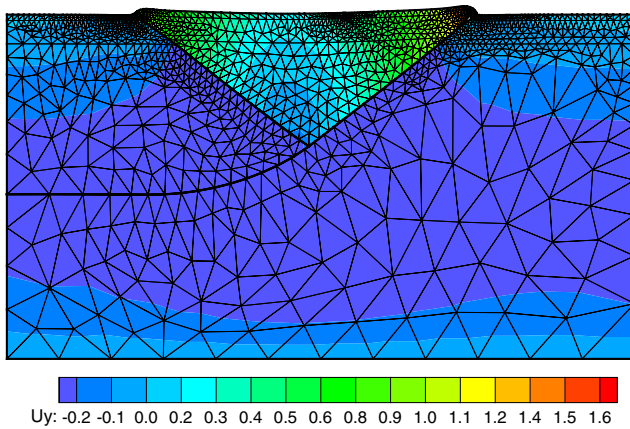


**Fig. 12** Deformed mesh with two faults 1 km deep after a horizontal contraction of 10.4 km (8.7% nominal strain). Initial dip  $\alpha_1 = \alpha_2 = 35^\circ$ ; coefficient of friction on the fault  $\mu = 0.577$ ; vertical displacement bar in kilometer

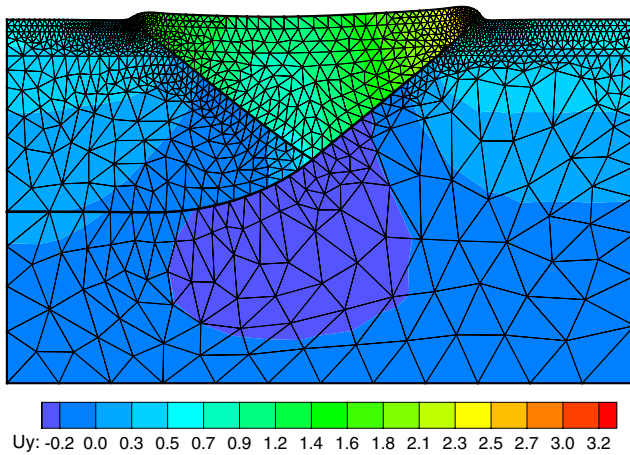


**Fig. 13** Deformed mesh with two faults 2 km deep after a horizontal contraction of 13.6 km (10.5% nominal strain). Initial dip  $\alpha_1 = \alpha_2 = 35^\circ$ ; coefficient of friction on the fault  $\mu = 0.577$ ; vertical displacement bar in kilometer

to propagate through the overlying ductile rock. If the overlying rock were brittle enough, then this material would fracture and the fault would emerge as a break on the Earth's surface.

In Fig. 15 we increase  $\alpha_2$  to  $45^\circ$  and again shorten the mesh by 10 km. Slip produced on the shorter fault is less even though slip produced on the primary fault remains essentially the same. If  $\alpha_2$  were reduced to a value less than  $35^\circ$ , then slip on the shorter fault would be greater. It may be argued therefore, that the degree of asymmetry of an anticline visible on the surface may be indicative of the combined effects of fault dip and fault depth, but unless one has confirmatory seismic reflection data it may be difficult to infer the length of a fault based on observed surface fold shapes alone.

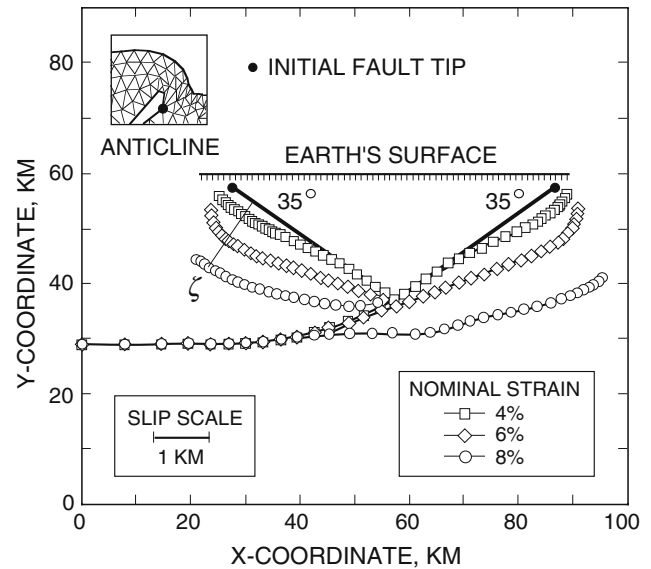


**Fig. 14** Spatial variation of tangential slip on fault axes for finite element mesh with two faults, having dips  $\alpha_1 = \alpha_2 = 35^\circ$ , and depth  $d = 1$  km. At any point on the fault the normal distance  $\zeta$  represents the cumulative tangential slip at that point on the fault. Note that contact elements around the tip experience an opening mode to allow an anticline to form. Boxed numbers in percent represent nominal horizontal strain

### 3.4 Effect of bulk plasticity around fault tip

So far we have assumed that the upper rock layer that folds without faulting deforms in a ductile manner. To better capture this behavior we model the stress-strain response of the two upper layers (layers 1 and 2) with an elastoplastic constitutive model. In this section we study the effect of plasticity on the geometry of the fold. We also carry out a bifurcation analysis to predict the emergence of deformation bands around the fault tip and on the fold itself. Our plasticity model utilizes the three-invariant Matsuoka-Nakai (MN) criterion to define plastic yielding [53], a non-associative flow rule, and a non-linear hardening law. This plasticity model has been incorporated into the finite element program via multiplicative plasticity [17]. The numerical integration of the constitutive law is done implicitly by a return mapping algorithm along the directions of the principal elastic stretches according to Borja et al. [17]. We investigate failure at each numerical integration point in the finite element model using the localization condition of Rudnicki and Rice [65]. Here we equate “failure” with the emergence of a deformation band. The localization condition entails tracking the evolution of the determinant function at each Gauss integration point, see Borja [10] for some algorithmic aspects. The onset of localization is then interpreted as the instant in the loading history at which this determinant function becomes equal to zero.

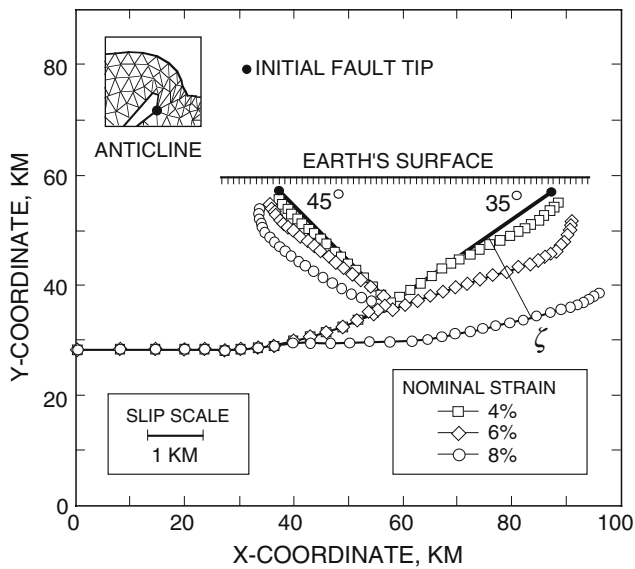


**Fig. 15** Spatial variation of tangential slip on fault axes for finite element mesh with two faults, having dips  $\alpha_1 = 35^\circ$  and  $\alpha_2 = 45^\circ$ , and depth  $d = 1$  km. At any point on the fault the normal distance  $\zeta$  represents the cumulative tangential slip at that point on the fault. Note the contact elements around the tip experience an opening mode to allow an anticline to form. Boxed numbers in percent represent nominal horizontal strain

The geometry and elastic parameters for this simulation are the same as those used in the analysis of an isolated primary fault. For the plasticity model we assume that the initial and final sizes of the MN yield surface correspond to friction angles of  $\varphi_i = 15^\circ$  and  $\varphi_f = 34^\circ$ , respectively, (friction hardening), and the dilatancy angle is  $\psi = 12^\circ$ . Note that these friction angles represent the bulk plasticity response, i.e., how fast the conical yield surface expands with the compressive mean normal stress, and have nothing to do with the friction angle on the fault. The ratio between the Young's modulus  $E$  and the cohesion  $c$  is  $E/c = 200$  for all rock layers.

Figure 16 shows contours of the localization function, defined as the minimum determinant of the elastoplastic acoustic tensor and used herein to detect the onset of deformation bands [65]. We predict localized deformations at the tip of the fault and on the forelimb of the fold. This mechanical instability is an indication of material damage. We infer that as a result of the material damage, fragments of rock would fill the gap produced by the contact elements around the fault tip as earlier postulated. While we are unable to simulate structural degradation and rock fragmentation with the standard finite element formulation used in this analysis, results of the bifurcation analysis indeed agree with an earlier statement that the region around the fault tip is a damage zone. As in the elastic case (Fig. 6), we have predicted an asymmetric anticline. However, the hinge curvature is now sharper, reflecting the ability of the more ductile material to transmit the shape of the advancing wedge corner. Since the upper elastoplastic layer experiences degradation of the tangent stiffness upon yielding, we predict greater structural relief for the same amount of horizontal contraction. Finally, the forelimb side of the anticline exhibits greater susceptibility to shear band instability. We have not checked the solution for diffuse instability such as cataclastic flow [12].

#### 4 Thrusting at Bighorn and Sheep Mountains

With insights gained from the generic problems of the previous section, we now apply the above modeling technique to analyze some aspects of thrust faulting on the flank of the Bighorn Basin in WY, USA. We shall be concerned primarily with Sheep Mountain Anticline (SMA), a Laramide-age doubly plunging anticline located in the foreland of the Rocky Mountains within the eastern Bighorn Basin of Wyoming. At SMA some exposed strata (typically sandstones and carbonates) are highly fractured

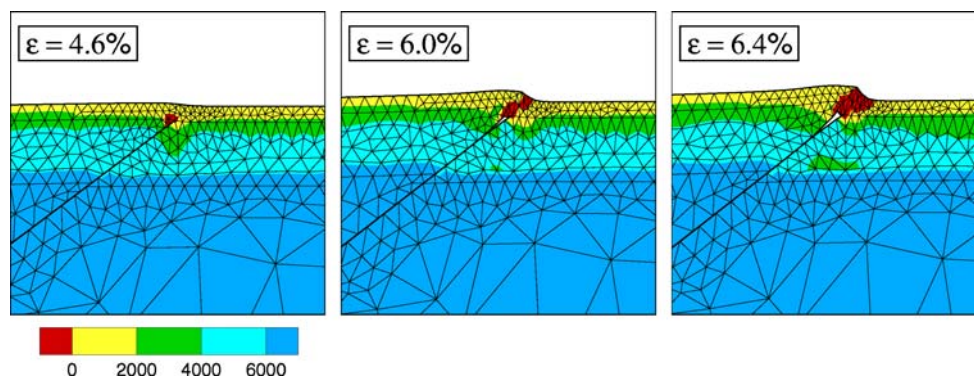


**Fig. 16** Snapshots of deformation from elastoplastic analysis with non-associative Matsuoka–Nakai yield criterion. Color contours denote intensity of localization function: red is probable zone of localized deformation, blue is probable zone of stable elastoplastic deformation. Initial fault depth  $d = 1$  km; initial dip  $\alpha_1 = 35^\circ$ ; coefficient of friction on the fault  $\mu = 0.577$ . Controlling variable  $\varepsilon$  is the nominal horizontal strain

whereas others (typically shales) apparently are not [7]. Nonetheless this package of strata is rarely cross cut and disrupted by minor faults. Therefore, we can take the uppermost layer above the tip of the fault to be sufficiently ductile so that it can fold when the underlying thrust fault slips. We shall also mention some notable structural features of thrusting related to the uplift of the Bighorn Mountains that we have been able to reproduce, at least qualitatively, with the proposed mechanical model.

Figure 17 shows a schematic cross section through the Bighorn Basin and Bighorn Mountains. The Bighorn Mountains consist of Archean granite overlain by Paleozoic platform rocks. The uplift is a fault block bounded by two great thrust faults: an uninterrupted, approximately 30°-dipping eastern thrust (e.g. the Piney Creek fault), and a shorter (about 20 km) approximately 30°-dipping western backthrust [80]. Slip on both thrusts induced by Laramide contractional deformation are substantial, although slip on the (longer) eastern thrust is greater. Save for scale, the uplifting of the Bighorn Mountains by the two faults as shown in Fig. 17 have been reproduced qualitatively in Figs. 12 and 13.

Figure 17 also shows the SMA thrust in the hanging wall of the Rio thrust fault (see Fig. 18 for an aerial view of SMA). Some believe that the Sheep Mountain fault is a third-order structure, arising as a backthrust of the Rio thrust fault, which in turn is believed to be a backthrust of the Bighorn Mountains Eastern Thrust [39, 41, 45, 79]. Figure 17 was adapted from Stone's [81] paper on the Torchlight Anticline that is similar to and along strike of SMA to the southeast.

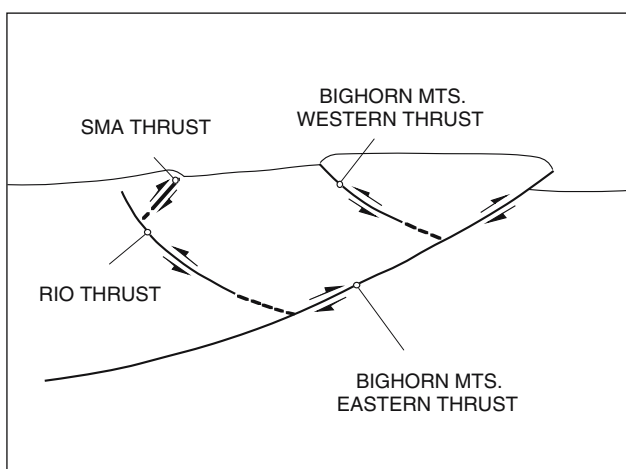


**Fig. 17** Schematic cross section through the Bighorn Basin and Bighorn Mountains showing the SMA as a third-order backthrust of the Rio thrust fault, which in turn is a backthrust of the Bighorn Mountains Eastern Thrust. Adapted from Stone [79, 80, 81] and reproduced from Fiore et al. [36]

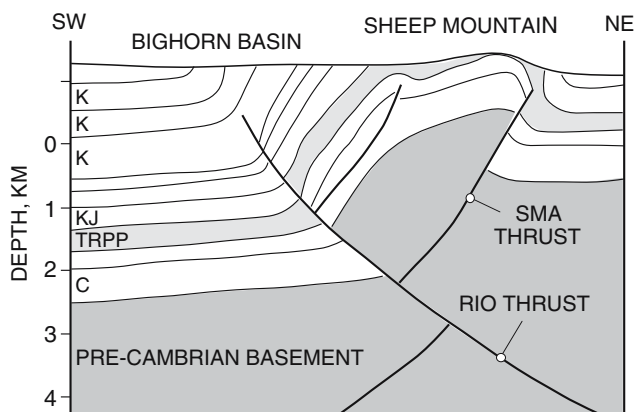
Current interpretations of the relationship between the Rio thrust fault and the SMA thrust fault conflict. Stanton and Erslev [76] investigated the fault geometry with the aid of two seismic reflection profiles perpendicular to, and one profile parallel to, the trend of Sheep Mountain. They built a 3D geometric model of the structure at Sheep Mountain and constructed 2D cross sections and 3D stratigraphic surfaces based on this geometric model. Figure 19 shows a SW-NE trending cross section through SMA based on the Stanton–Erslev geometric model and suggests that the Rio thrust fault slipped after the fault beneath SMA had already uplifted the fold. In other words, the interpretation of Stanton and Erslev is that the SMA fault is longer than suggested in Fig. 17, and that it is older than the Rio thrust, not a younger backthrust. Assuming the boundary condition defined by a far-field horizontal contraction represents the Laramide deformation and that the choices of model geometry and constitutive relations are reasonable approximations for this problem, we have used the finite element modeling technique to assess these two interpretations of the fold-thrust mechanism at Sheep Mountain.

Figure 20 shows the deformed mesh with two faults both 1 km deep. The mesh has the same resolution as in the previous simulations but we only show a close-up view of deformation around the fault tips. The longer fault represents the Rio thrust and the shorter one (approximately 6 km long) represents the SMA backthrust. The length and dip of the SMA thrust fault are the same order of magnitude as those used by Bellahsen et al. [6]. The figure shows that there is practically no fold near the tip of the SMA backthrust. In contrast significant folding takes place around the tip of the Rio thrust. This result shows that the SMA fault as represented in Fig. 17 is too short to significantly uplift and fold the rocks at Sheep Mountain.

Figure 20 can also be used to assess the Stanton–Erslev model (Fig. 19). If we remove the shorter fault and flip the



**Fig. 18** Aerial view of Sheep Mountain Anticline looking southeast. Anticline plunges to northwest



**Fig. 19** SW-NE trending cross-section through Sheep Mountain Anticline from Stanton and Erslev [76]. C Cambrian, TRPP Trias-Permian-Pennsylvanian, K Cretaceous, J Jurassic. The Stanton–Erslev model suggests that the Rio thrust fault slipped after slip along the fault beneath Sheep Mountain Anticline had already uplifted the fold. Reproduced from Bellahsen et al. [7]

figure 180 degrees, then the longer fault now takes the role of the (longer) SMA thrust fault *before* the Rio thrust fault had slipped. Because the SMA fault is now longer, it was able to uplift and fold the rocks at Sheep Mountain. We did not reproduce the subsequent rupturing of the Rio thrust fault as we lack information as to why the SMA fault deactivated and allowed the Rio thrust fault to slip and cut through it. However, Fig. 20 also suggests that if the Rio thrust did indeed slip after the SMA thrust had uplifted and folded the rock at Sheep Mountain, then the slip on the Rio thrust would not have significantly affected the geometric features of the uplifted anticline since the truncated SMA

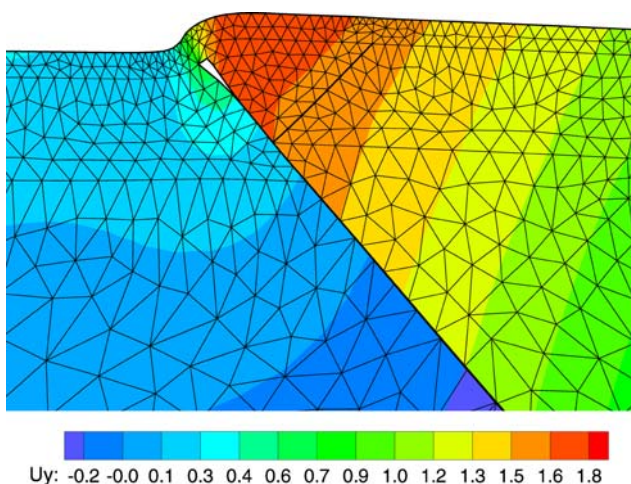


**Fig. 20** Deformed mesh with two faults 1 km deep after a horizontal contraction of 12 km (10% nominal strain). The primary fault represents the Rio thrust and the short fault represents the SMA backthrust approximately 6 km long. Initial dip  $\alpha_1 = \alpha_2 = 45^\circ$ ; coefficient of friction on the fault  $\mu = 0.577$ ; vertical displacement bar in kilometer

thrust would now be too short to cause significant additional deformation of the anticline.

## 5 Conclusions

Results presented in this paper suggest that under horizontal contraction, slip on a preexisting primary thrust fault depends strongly on the initial dip  $\alpha$ , coefficient of friction  $\mu$ , and the fault length. A greater dip  $\alpha$  and/or a greater coefficient of friction  $\mu$  may make thrusting more difficult, and depending on their combined effects a preexisting fault may or may not slip. If the existing fault could not slip, it is possible that a new fault would emerge with a more favorable orientation that is more conducive to sliding. Whether the overlying rock folds or faults depends on the magnitude of the slip relative to the depth of the primary fault, as well as on the ductility of the overlying layer. In case a fold is produced, underlying fault movement generally produces an asymmetric anticline. The shallower the fault and/or the flatter the dip, the more asymmetric the anticline. Results of the numerical simulations reveal that, in general, stretching and distortion are more pervasive on the forelimb side than on the backlimb side of an asymmetric anticline. Therefore, we can expect geomaterial damage (fractures, deformation bands, cataclastic flow, etc.) to be denser on the forelimb side than on the backlimb side of an asymmetric anticline.

Secondary thrust faults could significantly impact surface fold shapes if they are shallow and sufficiently long to generate significant slip. Like the primary fault, secondary thrust faults should be oriented favorably to permit sliding. Where the primary and secondary faults dip in opposite directions at about the same angle, simultaneous activation of the two faults could cause the entire wedge that is above them to thrust upward.

None of the mechanisms described above follows the principle of superposition commonly used in theory of elasticity; they can only be investigated by numerical modeling of a complex boundary-value problem. The work presented in this paper is a first step toward a more accurate modeling that ideally should include the effect of the third dimension and the irreversible deformation and fracturing of the rock. The proposed mechanical approach can also be seen as complementary to the geometric models of fold-thrust structures that cannot account for the strong influence of friction and material properties on the kinematics.

**Acknowledgments** We thank graduate students Fushen Liu for his assistance with plotting the deformed meshes and contours, and Tricia Fiore for her meticulous review of the Sheep Mountain Anticline section. This work is supported by National Science Foundation Grant No. CMG-0417521 (Collaborations in Mathematical Geosciences), and US Department of Energy Grant No. DE-FG02-03ER15454.

## References

1. Allmendinger RW (1988) Inverse and forward numerical modeling of trishear fault-propagation folds. *Tectonics* 17:640–656
2. Aydin A, Borja RI, Eichhubl P (2006) Geological and mathematical framework for failure modes in granular rock. *J Struct Geol* 28:83–98
3. Bai T, Pollard DD (2000) Fracture spacing in layered rocks: a new explanation based on the stress transition. *J Struct Geol* 22:43–57
4. Bai T, Pollard DD, Gao H (2000) Explanation for fracture spacing in layered materials. *Nature* 403:753–756
5. Beekman F, Badsı M, van Wees JD (2000) Faulting, fracturing and in situ stress prediction in the Ahnet basin, Algeria—a finite element approach. *Tectonophysics* 320:311–329
6. Bellahsen N, Fiore PE, Pollard DD (2006) From spatial variation of fracture patterns to fold kinematics: a geomechanical approach. *Geophys Res Lett* 33:L02301, doi:10.1029/2005GL024189
7. Bellahsen N, Fiore PE, Pollard DD (2006) The role of fractures in the structural interpretation of Sheep Mountain Anticline, Wyoming. *J Struct Geol* 28:850–867
8. Beutner EC, Diegel FA (1985) Determination of fold kinematics from syntectonic fibers in pressure shadows, Martinsburg Slate, New Jersey. *Am J Sci* 285:16–50
9. Borja RI (2000) A finite element model for strain localization analysis of strongly discontinuous fields based on standard Galerkin approximations. *Comput Meth Appl Mech Eng* 190:1529–1549
10. Borja RI (2002) Bifurcation of elastoplastic solids to shear band mode at finite strain. *Comput Meth Appl Mech Eng* 191:5287–5314
11. Borja RI (2002) Finite element simulation of strain localization with large deformation: capturing strong discontinuity using a Petrov–Galerkin multiscale formulation. *Comput Meth Appl Mech Eng* 191:2949–2978
12. Borja RI (2006) Conditions for instabilities in collapsible solids including volume implosion and compaction banding. *Acta Geotech* 1:107–122
13. Borja RI, Aydin A (2004) Computational modeling of deformation bands in granular media I: geological and mathematical framework. *Comput Meth Appl Mech Eng* 193:2667–2698
14. Borja RI, Foster CD (2007) Continuum mathematical modeling of slip weakening in geological systems. *J Geophys Res* (in press)
15. Borja RI, Lai TY (2002) Propagation of localization instability under active and passive loading. *J Geotech Geoenviron Eng* 128:64–75
16. Borja RI, Regueiro RA, Lai TY (2000) FE modeling of strain localization in soft rock. *J Geotech Geoenviron Eng* 126:335–343
17. Borja RI, Sama KM, Sanz PF (2003) On the numerical integration of three-invariant elastoplastic constitutive models. *Comput Meth Appl Mech Eng* 192:1227–1258
18. Bourne SJ (2003) Contrast of elastic properties between rock layers as a mechanism for the initiation and orientation of tensile failure under remote compression. *J Geophys Res* 108:2395
19. Bump AP (2003) Reactivation, trishear modeling, and folded basement in Laramide uplifts: implications for the origins of intra-continental faults. *Geol Soc Am* 13:4–10
20. Cardozo N, Bawa-Bhalla K, Zehnder A, Allmendinger RW (2003) Mechanical models of fault propagation folds and comparison to the trishear kinematic model. *J Struct Geol* 25:1–18
21. Cardozo N, Allmendinger RW, Morgan JK (2005) Influence of mechanical stratigraphy and initial stress state on the formation of two fault propagation folds. *J Struct Geol* 27:1954–1972
22. Carena S, Suppe J (2002) Three-dimensional imaging of active structures using earthquake aftershocks: the Northridge Thrust, California. *J Struct Geol* 24:887–904
23. Cooke ML, Underwood CA (2001) Fracture termination and step-over at bedding interfaces due to frictional slip and interface opening. *J Struct Geol* 23:223–238
24. Cooke M, Mollema P, Pollard DD, Aydin A (2000) Interlayer slip and joint localization in East Kaibab Monocline, Utah: field evidence and results from numerical modeling. In: Cosgrove JW, Ameen MS (eds) *Forced folds and fractures*. Geological Society Special Publication, London, pp 23–49
25. Cristallini EO, Allmendinger RW (2002) Pseudo 3-D modelling of trishear fault-propagation folding. *J Struct Geol* 23:1883–1899
26. Cruikshank KM, Aydin A (1995) Unweaving the joints in Entrada Sandstone, Arches National Park, Utah, USA. *J Struct Geol* 17:409–421
27. Cruikshank KM, Zhao G, Johnson AM (1991) Analysis of minor fractures associated with joints and faulted joints. *J Struct Geol* 13:865–886
28. Dieterich JH (1979) Modeling of rock friction 1. Experimental results and constitutive equations. *J Geophys Res* 84:2161–2168
29. Dolbow J, Moes N, Belytschko T (2001) An extended finite element method for modeling crack growth with frictional contact. *Comput Meth Appl Mech Eng* 190:6825–6846
30. Engelder T, Peacock DCP (2001) Joint development normal to regional compression during flexural-flow folding: the Lilstock buttress anticline, Somerset, England. *J Struct Geol* 23:259–277
31. Erickson SG, Jamison WR (1995) Viscous-plastic finite-element models of fault-bend folds. *J Struct Geol* 17:561–573
32. Erickson SG, Strayer LM, Suppe J (2001) Initiation and reactivation of faults during movement over a thrust-fault ramp: numerical mechanical models. *J Struct Geol* 23:11–23
33. Erslev EA (1991) Trishear fault-propagation folding. *Geology* 19:617–620
34. Finch E, Hardy S, Gawthorpe R (2003) Discrete element modeling of contractional fault-propagation folding above rigid basement fault blocks. *J Struct Geol* 25:515–528
35. Fiore PE (2006) 3D characterization and mechanics of brittle deformation in thrust fault related folds. PhD thesis, Stanford University, Calif, USA
36. Fiore PE, Bellahsen N, Pollard DD (2006) The rock fracture project field trip, Sheep Mountain Anticline, WY. Rock Fracture Project, Stanford University, California
37. Fiore PE, Pollard DD, Currin W, Miner DM (2006) Mechanical and stratigraphic constraints on the evolution of faulting at Elk Hills, CA. *AAPG Bulletin* (in press)
38. Fischer MP, Wilkerson MS (2000) Predicting the orientation of joints from fold shape: results of pseudo-three-dimensional modeling and curvature analysis. *Geology* 28:15–18
39. Forster D, Irmen AP, Vondra C (1996) Structural interpretation of Sheep Mountain Anticline, Bighorn Basin, Wyoming. *Wyo Geol Assoc Guideb* 47:239–251
40. Goangseup Z, Belytschko T (2003) New crack-tip elements for XFEM and applications to cohesive cracks. *Int J Numer Meth Eng* 57:2221–2240
41. Gries R (1983) Oil and gas prospecting beneath Precambrian of foreland thrust plates in the Rocky Mountains. *Am Assoc Petrol Geol Bull* 67:1–28
42. Gutierrez-Alonso G, Gross MR (1999) Structures and mechanisms associated with development of a fold in the Cantabrian Zone thrust belt, NW Spain. *J Struct Geol* 21:653–670
43. Hardy S, Finch E (2006) Discrete element modeling of the influence of the cover strength on basement-involved fault-propagation folding. *Tectonophysics* 415:225–238
44. Henk A (2006) Stress and strain during fault-controlled lithospheric extension: Insights from numerical experiments. *Tectonophysics* 415:39–55

45. Hennier J, Spang J (1983) Mechanisms for deformation of sedimentary strata at Sheep Mountain Anticline, Big Horn Basin, Wyoming. *Wy Geol Assoc Guideb* 34:97–111
46. Jackson MD, Pollard DD (1988) The laccolith-stock controversy: new results from the southern Henry Mountains, Utah. *Geol Soc Am Bull* 100:117–139
47. Jamison WR (1987) Geometric analysis of fold development in overthrust terranes. *J Struct Geol* 9:207–219
48. Johnson KM, Johnson AM (2000) Localization of layer-parallel faults in San Rafael swell, Utah and other monoclinical folds. *J Struct Geol* 22:1455–1468
49. Lapusta N (2005) Modes of dynamic rupture propagation and rupture front speeds in earthquake models that account for dynamic weakening mechanisms. *EOS Trans AGU* 86(52), Fall Meet Suppl, Abstract S34A-07
50. Laursen TA, Simo JC (1993) A continuum-based finite element formulation for the implicit solution of multibody, large deformation frictional contact problems. *Int J Num Meth Eng* 36:3451–3485
51. Luenberger DG (1984) *Linear and nonlinear programming*, 2nd edn. Addison-Wesley, Reading
52. Malvern LE (1969) *Introduction to the mechanics of a continuous medium*. Prentice-Hall, Inc, Englewood Cliffs, New Jersey
53. Matsuoka H, Nakai T (1974) Stress-deformation and strength characteristics of soil under three different principal stresses. *Proc JSCE* 232:59–70
54. McConaughy DT, Engelder T (2001) Joint initiation in bedded clastic rocks. *J Struct Geol* 23:203–221
55. McConnell D (1994) Fixed-hinge, basement-involved fault-propagation folds, Wyoming. *Geol Soc Am Bull* 106:1583–1593
56. Mitra S (1990) Fault-propagation folds: geometry, kinematic evolution, and hydrocarbon traps. *Am Assoc Petrol Geol Bull* 74:921–945
57. Moes N, Belytschko T (2002) Extended finite element method for cohesive crack growth. *Eng Fract Mech* 69:813–833
58. Niño F, Philip H, Chery J (1998) The role of bed-parallel slip in the formation of blind thrust faults. *J Struct Geol* 20:503–516
59. Nour-Omid B, Wriggers P (1987) A note on the optimum choice for penalty paramters. *Commun Appl Numer Methods* 3:581–585
60. Ogden RW (1984) *Non-linear elastic deformations*. Ellis Harwood Ltd., Chichester, UK
61. Regueiro RA, Borja RI (2001) Plane strain finite element analysis of pressure-sensitive plasticity with strong discontinuity. *Int J Solids Struct* 38:3647–3672
62. Rice JR (2006) Heating and weakening of faults during earthquake slip. *J Geophys Res* 111:B05311
63. Riley DJ (1996) Applications of numerical modeling to thrust tectonics. Ph.D. thesis, University of Southampton
64. Rivero C, Shaw JH, Mueller K (2000) Oceanside and Thirtymile Bank blind thrusts: implications for earthquake hazards in coastal southern California. *Geology* 28:891–894
65. Rudnicki JW, Rice JR (1975) Conditions for the localization of deformation in pressure-sensitive dilatant materials. *J Mech Phys Solids* 23:371–394
66. Ruina AL (1983) Slip instability and state variable friction laws. *J Geophys Res* 88:10359–10370
67. Savage HM, Cooke ML (2003) Can flat-ramp-flat fault geometry be inferred from fold shape? A comparison of kinematic and mechanical folds. *J Struct Geol* 25:2023–2034
68. Savage HM, Cooke ML (2004) The effect of non-parallel thrust fault interaction on fold patterns. *J Struct Geol* 26:905–917
69. Scholz CH (1990) *The mechanics of earthquakes and faulting*. Cambridge University Press, Cambridge
70. Schultz RA (1999) Understanding the process of faulting: selected challenges and opportunities at the edge of the 21st century. *J Struct Geol* 21:985–993
71. Shamir G, Eyal Y (1995) Elastic modeling of fault-driven monoclinical fold patterns. *Tectonophysics* 245:13–24
72. Simo JC, Laursen TA (1992) An augmented Lagrangian treatment of contact problems involving friction. *Comput Struct* 42:97–116
73. Smart KJ, Krieg RD, Dunne WM (1999) Deformation behavior during blind thrust translation as a function of fault strength. *J Struct Geol* 21:855–874
74. Smith JV, Marshall B (1992) Patterns of imbricate folding and fold interference in oblique contraction of layered rocks of the inverted Cobar Basin, Australia. *Tectonophysics* 215:319–335
75. Spang JH, McConnell DA (1997) Effect of initial geometry on the development of fixed-hinge, fault-propagation. *J Struct Geol* 19:1537–1541
76. Stanton HI, Erslev EA (2004) Sheep Mountain: backlimb tightening and sequential deformation in the Bighorn Basin, Wyoming. *Wyo Geol Assoc Guideb* 54:75–87
77. Stein RS, Barrientos SE (1985) Planar high-angle faulting in the Basin and Range: geodetic analysis of the 1983 Borah Peak, Idaho, Earthquake. *J Geophys Res* 90:11355–11366
78. Stein RS, Yeats RS (1989) Hidden earthquakes. *Sci Am* 260:48–57
79. Stone DS (1993) Basement-involved thrust generated folds as seismically imaged in sub-surface of the central Rocky Mountain foreland. In: Schmidt CJ, Chase RB, Erslev EA (Eds) *Laramide basement deformation in the Rocky Mountain Foreland of the Western United States*. Geological Society of America Paper 280, pp 271–318
80. Stone DS (2003) New interpretations of the Piney Creek thrust and associated Granite Ridge tear fault, northeastern Bighorn Mountains, Wyoming. *Rocky Mt Geol* 38:205–235
81. Stone DS (2004) Rio thrusting, multi-stage migration, and formation of vertically segregated Paleozoic oil pools at Torchlight Field on the Greybull Platform (Eastern Bighorn Basin): implications for exploration. *Mt Geol* 41:119–138
82. Strayer LM, Hudleston PJ (1997) Numerical modeling of fold initiation at thrust ramps. *J Struct Geol* 19:551–566
83. Strayer LM, Suppe J (2002) Out of plane motion of a thrust sheet during along-strike propagation of a thrust ramp: a distinct element approach. *J Struct Geol* 24:637–650
84. Suppe J (1983) Geometry and kinematics of fault-bend folding. *Am J Sci* 283:684–721
85. Suppe J (1985) *Principles of structural geology*. Prentice-Hall, Inc, Englewood Cliffs, New Jersey
86. Suppe J, Medwedeff DA (1990) Geometry and kinematics of fault-propagation folding. *Ecol Geol Helv* 83:409–454
87. Treagus SH (1988) Strain refraction in layered systems. *J Struct Geol* 10:517–527
88. Tse ST, Rice JR (1986) Crustal earthquake instability in relation to the variation of frictional slip properties. *J Geophys Res* 91:9452–9472
89. Wilkins SJ, Gross MR, Wacker M, Eyal Y, Engelder T (2001) Faulted joints: kinematics, displacement-length scaling relations and criteria for their identification. *J Struct Geol* 23:315–327
90. Wriggers P (1995) Finite element algorithms for contact problems. *Arch Comput Methods Eng* 4:1–49
91. Wriggers P (2002) *Computational contact mechanics*. Wiley, Chichester
92. Wriggers P, Van TV, Stein E (1990) Finite-element-formulation of large deformation impact-contact-problems with friction. *Comput Struct* 37:319–333
93. Xing HL, Makinouchi A (2002) Finite-element modeling of multibody contact and its application to active faults. *Concurr Comput Pract Exp* 14:431–450